Proceedings of the Fifteenth International Conference on
Computational Structures Technology
Edited by: P. Iványi, J. Kruis and B.H.V. Topping
Civil-Comp Conferences, Volume 9, Paper 3.2
Civil-Comp Press, Edinburgh, United Kingdom, 2024
ISSN: 2753-3239, doi: 10.4203/ccc.9.3.2

Topology Optimization Method for High-Aspect-Ratio Wing Considering Geometrical Nonlinearity with Directional Length Scale Control

L. Song, Y. Li, Y. Huang, P. Fang, T. Gao and W. Zhang

School of Mechanical Engineering, Northwestern Polytechnical University
Xi'an, China

Abstract

The high-aspect-ratio wing, which is widely utilized in aircraft to achieve superior aerodynamic efficiency, frequently experiences large deformations during its service life. This work focuses on the topology optimization of the high-aspect-ratio wing using multiple materials considering geometric nonlinearity. To produce the spar-ribs structural layout, the directional length scale control is introduced by utilizing cylinder local search instead of conventional circle local search in the framework of the multi-material topology optimization. The Neo-Hookean hyperelastic model is utilized to characterize the behavior of the original material to alleviate the numerical difficulties caused by geometric nonlinearity. Finally, the high-aspect-ratio wing is optimized and the results demonstrate that the spar-ribs structural layout is achieved with the directional length scale control.

Keywords: topology optimization, high-aspect-ratio wing, geometric nonlinearity, directional length scale control, multiple materials, spar-ribs structural layout.

1 Introduction

To pursue high aerodynamic efficiency, the high-aspect-ratio wing is widely applied on aircraft due to the increase in lift-to-drag ratio. This is particularly evident in solar-powered UAVs (Unmanned Aerial Vehicle). According to engineering practice, the high-aspect-ratio wing typically exhibits four key characteristics: (i) The spar-ribs structural layout remains the preferred configuration for the high-aspect-ratio wing, like the Helios[1] and Solar Impulse[2]. (ii) These wings normally endure significant deformation, particularly in the forms of (iii) bending and torsion. (iii) Multiple

materials are commonly utilized, as in solar-powered UAVs where the materials for the main spar and wing ribs may vary.

The consideration of multi-material topology optimization is essential to expand the design space. In recent decades, there has been a notable surge of attention in multi-material topology optimization. Under the framework of the density-based methods, an interpolation scheme rooted in the rule of mixtures to characterize the distribution of multiple materials was introduced by Bendsøe et al.[3].

In this paper, we focus on the topology optimization of the high-aspect-ratio wing under large deformation considering bending and torsion control. In the framework of the three-field approach, the multi-material topology optimization method is developed based on the uniform multiphase materials interpolation (UMMI) scheme[4]. Considering the geometrical nonlinearity, the end-compliance is utilized as the objective function. Both bending and torsion controls are introduced as constraints and defined as functions of the nodal displacement field. The sensitivity analysis is derived by extracting the increment of nodal displacement. Besides, the directional maximum length scale control is employed for the void phase to achieve a spar-ribs material layout.

2 Methods

2.1 Three-field approach and length scale control

The three-field approach employed in multi-material topology optimization consists of the design variable field $\mathbf{x}$, filtered density field $\tilde{\mathbf{x}}$, and physical density field $\overline{\mathbf{x}}$. The filtered field is calculated with the operation of the design variable field and filter matrix, which is related to the distance weight. The expression based on the tanh function is utilized for the filtered field to obtain the projected field. The details of their relations can be referenced in the previous work[5].

The interpolation of Young's modulus of *i*-th element based on UMMI scheme is obtained with the weighted sum of all candidate materials.

$$E_i = \sum_{j=1}^{m} \lambda_{ij} E^{(j)}, \tag{1}$$

where m is the number of candidate materials, $E^{(j)}$ is the Young's modulus of j-th material. λ_{ij} is the weighting function of the physical variable $\overline{x}_{ij}$, which can be presented as

$$\lambda_{ij} = \overline{x}_{ij}^{p} \prod_{\substack{\xi=1 \\ \xi \neq j}}^{m} \left(1 - \overline{x}_{i\xi}^{p}\right), \tag{2}$$

in which p is the penalty factor for the design variable.

The local material rate of material j is introduced in the local search domain to achieve the maximum length scale control for the void phase as presented in Fig. 1, which is defined as

$$\psi_i^{(j)} = \frac{\sum_{k\in\Omega_i} v_k \bar{x}_{kj}^{p}}{\sum_{k\in\Omega_i} v_k}. \tag{3}$$

To achieve the spar-ribs configuration in the wing, we utilize cylinder local search instead of conventional circle local search for directional maximum length scale control of a single void phase, as illustrated in Fig 2. The length of the cylinder search domain, l, is set equal to the distance between adjacent ribs. To ensure a single-strip element in the local search domain, the diameter of the cylinder should not exceed the length of the element.

The biasing and aggregation of Eq. (3) processed to a global constraint can be found in previous works[5, 6]. Additionally, the cylinder local search reduces the computational costs including the local search time and the occupied memory as demonstrated in [6].

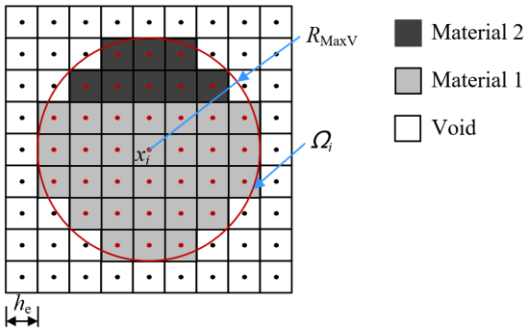

Fig. 1 Conventional circle local search with the local material rate of material 1: $\psi_i^{(1)} = 78.38\%$

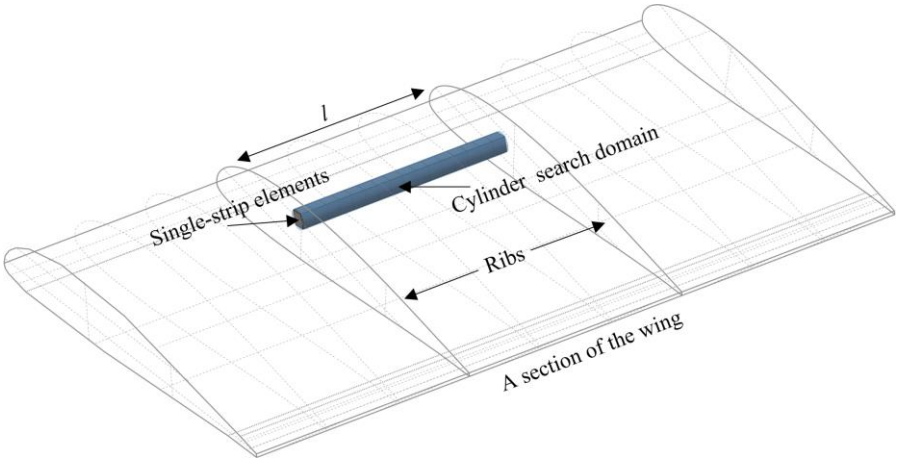

Fig. 2 Cylinder local search for the directional maximum length scale control

2.2 Finite element formulation for geometrical nonlinearity

The commercial FEA has the advantages of speed and extensibility, especially for engineering structures. The commercial ANSYS solver is utilized in this work. However, it's hard to achieve the energy interpolation scheme [7] as the tangent stiffness matrix cannot be obtained from the commercial software. On the other hand,

the calculation scale doubles when using the additive hyperelasticity technique [8, 9] and it's not cost-effective for engineering problems. Thus the Neo-Hookean model is utilized to characterize the behavior of the original material and its strain energy potential of the Neo-Hookean model in ANSYS is defined as

$$\phi_{\text{neo}} = \frac{G}{2}(\bar{I}_1 - 3) + \frac{1}{d}(J-1)^2, \tag{4}$$

where G is the initial shear modulus of candidate materials, $\bar{I}_1$ is the first deviatoric strain invariant, J is the determinant of the elastic deformation gradient, d is the material incompressibility parameter given by $d = 2/K$, and K is the initial bulk modulus. Thus we can obtain the following form of the Neo-Hookean model corresponding to the elastic modulus E.

$$\phi_{\text{neo}} = E\left(\frac{1}{4(1+\upsilon)}(\bar{I}_1 - 3) + \frac{1}{6(1-2\upsilon)}(J-1)^2\right), \tag{5}$$

in which υ is the Poisson's ratio. The strain energy of i-th element can be calculated as

$$Q_i = \int_{V_i} \phi_{\text{neo}}(E_i)\mathrm{d}V, \tag{6}$$

where V_i is the volume of the i-th element. The Newton-Raphson method is normally applied in FEA and the incremental equation can be expressed as

$$\mathbf{r} = \mathbf{K}_{\text{T}}\Delta\mathbf{u}, \tag{7}$$

where $\mathbf{r}$ and $\mathbf{K}_{\text{T}}$, are the global residual force vector and the tangent stiffness matrix, respectively. The global displacement vector $\mathbf{u}$ is updated with $\mathbf{u} = \mathbf{u} + \Delta\mathbf{u}$. Repeat iteration Eq. (7) until $\mathbf{r}$ reaches zero or an acceptably small value to obtain a converged solution.

$$\mathbf{r} = \mathbf{f}^{\text{ext}} - \mathbf{f}^{\text{int}}(\bar{\mathbf{x}}, \mathbf{u}) = \mathbf{0}. \tag{8}$$

Herein, $\mathbf{f}^{\text{ext}}$ and $\mathbf{f}^{\text{int}}$ are the external and internal nodal load vector, respectively.

2.3 Optimization formula

In topology optimization with geometrical nonlinearity, the objective function typically involves minimizing the structural complementary elastic work and end-compliance. In this work, ANSYS is employed for FEA, and iterative displacement in the Newton-Raphson method is not attainable. Consequently, the end-compliance function is utilized and expressed as follows:

$$C = \mathbf{P}^{\text{T}}\mathbf{u}_N, \tag{9}$$

which is computed solely in the final equilibrium, i.e., during the N-th incremental load step. $\mathbf{P}$ is the external force vector and is expressed by $\mathbf{P} = \mathbf{f}^{\text{ext}}$.

Based on multi-material topology optimization, the problem of minimizing end-compliance, while considering geometric nonlinearity and subject to constraints on structural mass, volume, and length scale control, is formulated as

$$
\begin{aligned}
&\text{find}: && \mathbf{x} = \left\{ x_{ij} \right\} \ (i = 1,...,n;\ \ j = 1,...,m) \\
&\text{minmize}: && C = \mathbf{P}^{\mathrm{T}} \mathbf{u}_N \\
&\text{subject to}: && \mathbf{r}(\bar{\mathbf{x}}, \mathbf{u}) = \mathbf{f}^{\mathrm{int}} - \mathbf{f}^{\mathrm{ext}} = \mathbf{0} \\
& && \bar{\mathbf{x}}^{(j)} = H(\hat{\mathbf{x}}^{(j)}) = H(\mathbf{W}\mathbf{x}^{(j)}) \\
& && M = \sum_{n=1}^{n} \sum_{j=1}^{m} \bar{x}_{ij}^{p_{\mathrm{D}}} \rho^{(j)} V_i \le \bar{M} \\
& && V_{\mathrm{f}}^{(j)}(\bar{\mathbf{x}}) = \sum_{i=1}^{n} \bar{x}_{ij} V_i \le f_{\mathrm{U}}^{(j)} \cdot V_0 \\
& && G_{\mathrm{MaxV}} < 0 \\
& && 0 < x_{\min} \le x_{ij} \le 1
\end{aligned}
\quad , \tag{10}
$$

herein, H is the Heaviside function and $\mathbf{W}$ is the filter matrix. M is the structural mass, which should be less than the upper bound $\bar{M}$. $\rho^{(j)}$ denotes the material density related to the j-th material and p_{D} is the penalty factor for densities. $V_{\mathrm{f}}^{(j)}$ and $f_{\mathrm{U}}^{(j)}$ are the volume of the j-th material and the prescribed upper bound of the volume fraction, respectively. G_{MaxV} represents the directional maximum length scale control for the void phase. To prevent the solver from getting trapped in an nonconvergent solution due to large deformation at the initial stage of optimization, the densities of the candidate materials are penalized. As a result, the optimization begins with a high initial value of variables.

3 Results

In this section, the proposed method is employed on a straight wing with a 16:1 aspect ratio, subject to aerodynamic pressure. One side of the wing is illustrated in Fig. 3. The skin of the wing is treated as a non-design domain and is meshed with 39040 shell elements. Meanwhile, the interior of the wing is defined as the design domain, which is discretized with 100800 hexahedral elements.

According to engineering practice, two equivalent candidate composite materials Mat1 and Mat2 are used and the related materials properties are presented in Table 1. These two materials have the same density although the performance of both stiffness and strength are different. Mat1 is chosen for the main spar for its high Young's modulus, while Mat2 is employed for ribs. The cruising speed of the solar-powered drone is normally below 100 m/s, such as the average cruising speed of Zephyr[10] is around 10 m/s. The aerodynamic pressure of the wing is obtained from CFD analysis. The contours under speeds of 10 and 100 m/s are shown in Fig. 3 (b) and (c), respectively. Notably, the optimization is processed under the assumption that the aerodynamic pressure remains constant in the iterations. The nodes on the wing root section are fixed.

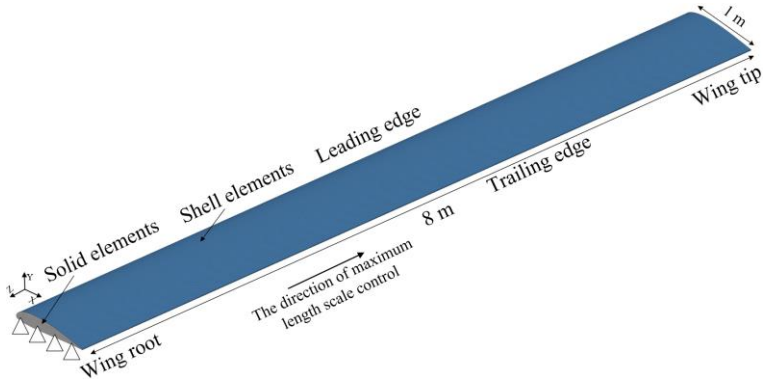

(a) the mesh: 100800 hexahedral elements and 39040 shell elements

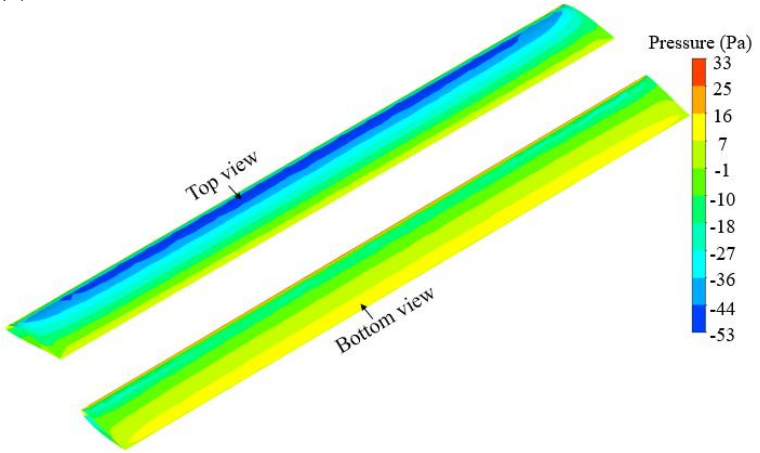

(b) the aerodynamic load at a speed of 10 m/s

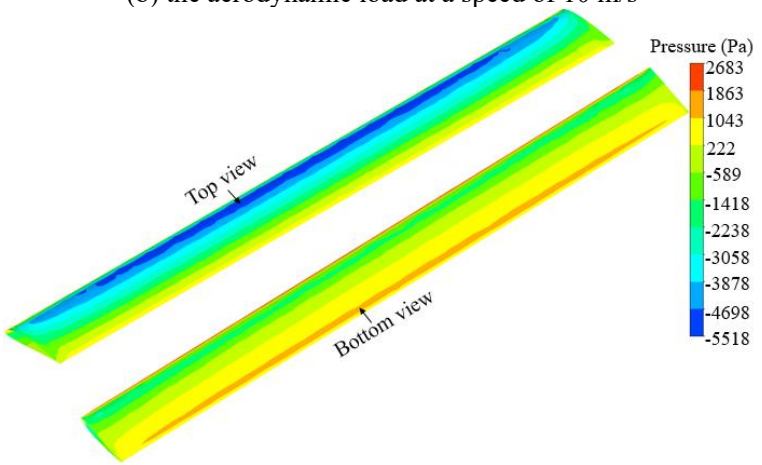

(c) the aerodynamic load at a speed of 100 m/s

Fig. 3 The mesh and the aerodynamic load of the high-aspect-ratio wing

The upper bounds of total structural mass and volume fraction of MAT2 are set as $\bar{M} = 350$ kg and $\bar{V}_{\mathrm{f}}^{(\mathrm{Mat2})} = 0.15$. The filter radius is set as $R_f = 2\ h_e$, which h_e is the size of the element. To avoid the impact of the projection on the optimization configuration, an incremental change way for the Heaviside projection coefficient β is utilized. It is 1 for the first 50 iterations and then is increased from 2 to 32 with a multiplying factor of 1.3 for every 10 iterations. The penalty factor p_D for material

densities is set at the value of 1.5. Additionally, the move limit should be sufficiently small, and a value of 0.02 is set for the iterative solution.

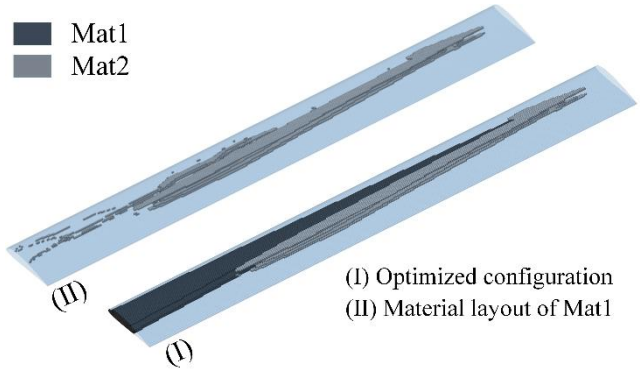

(a) with a speed of 10 m/s

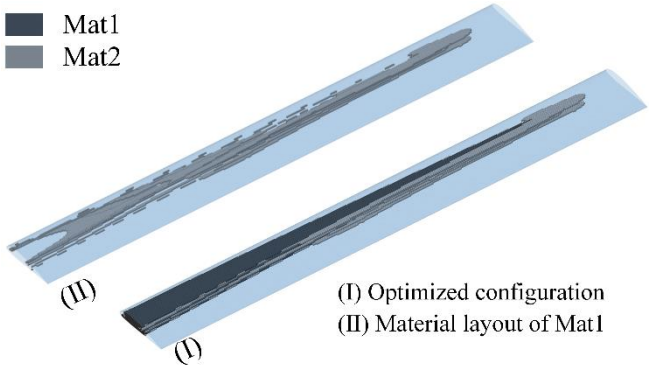

(b) with a speed of 100 m/s

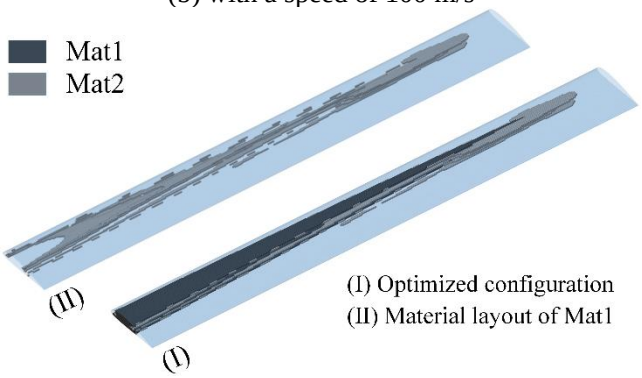

(c) with 300 times the aerodynamic loads at 10 m/s

Fig. 4 The optimized results of the minimization of the end-compliance with different aerodynamic loads

To combine the conventional spar-ribs layout, the directional maximum length scale control with a ϕ 0.02×0.4 m cylinder search for the void phase of MAT2 is imposed to the optimization. The direction of the length scale control is along the wingspan as shown in Fig. 3 (a).

The optimized results of the minimization of the end-compliance with different aerodynamic loads are presented in Fig. 4. The material layouts of the optimized configurations are different from the aerodynamic loads. The weak material Mat 2 is

more likely to distribute at wing root and wing tip and its usage decreases with a larger aerodynamic load. This demonstrates the topology optimization considering geometric nonlinearity works in this work.

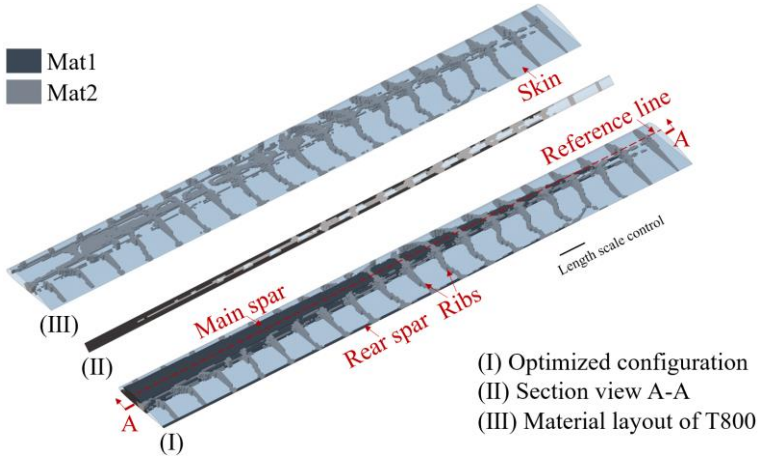

(a) ϕ 0.02×0.4 m

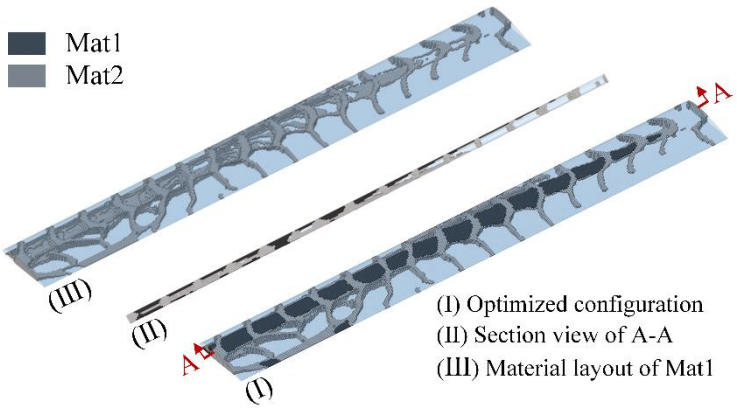

(b) ϕ 0.02×0.5 m

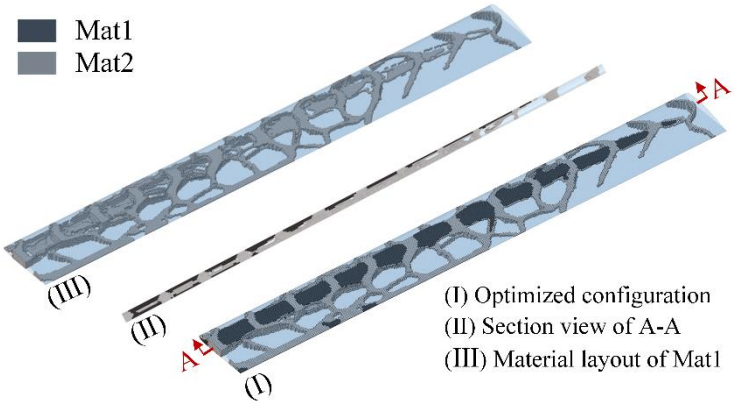

(c) ϕ 0.02×0.6 m

Fig. 5 The optimized results of the minimization of the end-compliance with different sizes of local cylinder search

The directional maximum length scale control for the Mat 2 void phase is imposed to the optimization under the aerodynamic load with a speed of 100 m/s (Fig.

4 (b)). Three tests with different sizes ϕ 0.02×0.4 m, ϕ 0.02×0.5 m, ϕ 0.02×0.6 m for directional maximum length scale control are optimized and the results are shown in Fig. 5. The spar-ribs layouts distribute when the directional length scale control is considered and vary from the length of local cylinder search. The main spar, rear spar, and ribs distinctly distributed in all optimized results. Notably, the main spar consists of a laminated structure incorporating both materials, with its dimensions tapering from the wing root to the wing tip. Additionally, the centerline of the main spar slightly shifts toward the trailing edge of the wing nearing the wing tip, as indicated by the reference line. The more regular spar-ribs layout can be obtained under a size of ϕ 0.02×0.4 m for local cylinder search.

4 Conclusions and Contributions

The multi-material topology optimization for a high-aspect-ratio straight wing with directional maximum length scale control while considering the geometric nonlinearity is developed. Directional maximum length scale control based on a local material rate for a single void phase is employed to improve the manufacturability of the wing. The proposed methods are successfully applied to the high-aspect-ratio wing. The optimized results show that the multi-material topology optimization considering geometric nonlinearity with directional length scale control expands the design space and achieves material spar-ribs layout for the wing. The novel optimized material layout contains regular ribs, the main spar, and the rear spar.

The optimized spar-ribs structural schemes in this work move towards practical engineering and exhibit manufacturing friendliness. This can be achievable through the implementation of truss structures that hold significant potential in lightweight designs for the high-aspect-ratio wing. For future work, extension to large-scale problems will be processed, where the computational efficiency of iterative solutions for the nonlinear problem is the main focus. Furthermore, the potential applications of the proposed approach on the high-aspect-ratio wing will be pursued to enable a more detailed and comprehensive design.

Acknowledgements

This work is supported by the National Key Research and Development Program of China (2022YFB4602001).

References

[1] T. Tschida, Technician Marshall MacCready installs solar cells on the Helios prototype, (2000).
[2] D. Dawson, Solar Impulse 2: pulse on the future, Composites World, 71 (2016) 36–53.
[3] M.P. Bendsøe, O. Sigmund, Material interpolation schemes in topology optimization, Arch Appl Mech, 69 (1999) 635-654.
[4] T. Gao, W.H. Zhang, A mass constraint formulation for structural topology optimization with multiphase materials, Int J Numer Meth Eng, 88 (2011) 774-796.

[5] L.L. Song, J. Zhao, T. Gao, J.J. Li, L. Tang, Y. Li, W.H. Zhang, Length scale control in density-based multi-material topology optimization, Computer Methods in Applied Mechanics and Engineering, 401 (2022) 115655.
[6] L.L. Song, T. Gao, J. Wang, W.H. Zhang, Directional maximum length scale control in density-based topology optimization, Computers & Structures, 292 (2024) 107236.
[7] F.W. Wang, B.S. Lazarov, O. Sigmund, J.S. Jensen, Interpolation scheme for fictitious domain techniques and topology optimization of finite strain elastic problems, Computer Methods in Applied Mechanics and Engineering, 276 (2014) 453-472.
[8] Q. Chen, X. Zhang, B. Zhu, A 213-line topology optimization code for geometrically nonlinear structures, Structural and Multidisciplinary Optimization, 59 (2019) 1863-1879.
[9] Y.J. Luo, M.Y. Wang, Z. Kang, Topology optimization of geometrically nonlinear structures based on an additive hyperelasticity technique, Computer Methods in Applied Mechanics and Engineering, 286 (2015) 422-441.
[10] A. Rapinett, Zephyr: A High Altitude Long Endurance Unmanned Air Vehicle. University of Surrey, 2009.